iScience

CellPress
OPEN ACCESS

Article

A new polymorphism of human amylin fibrils with similar protofilaments and a conserved core

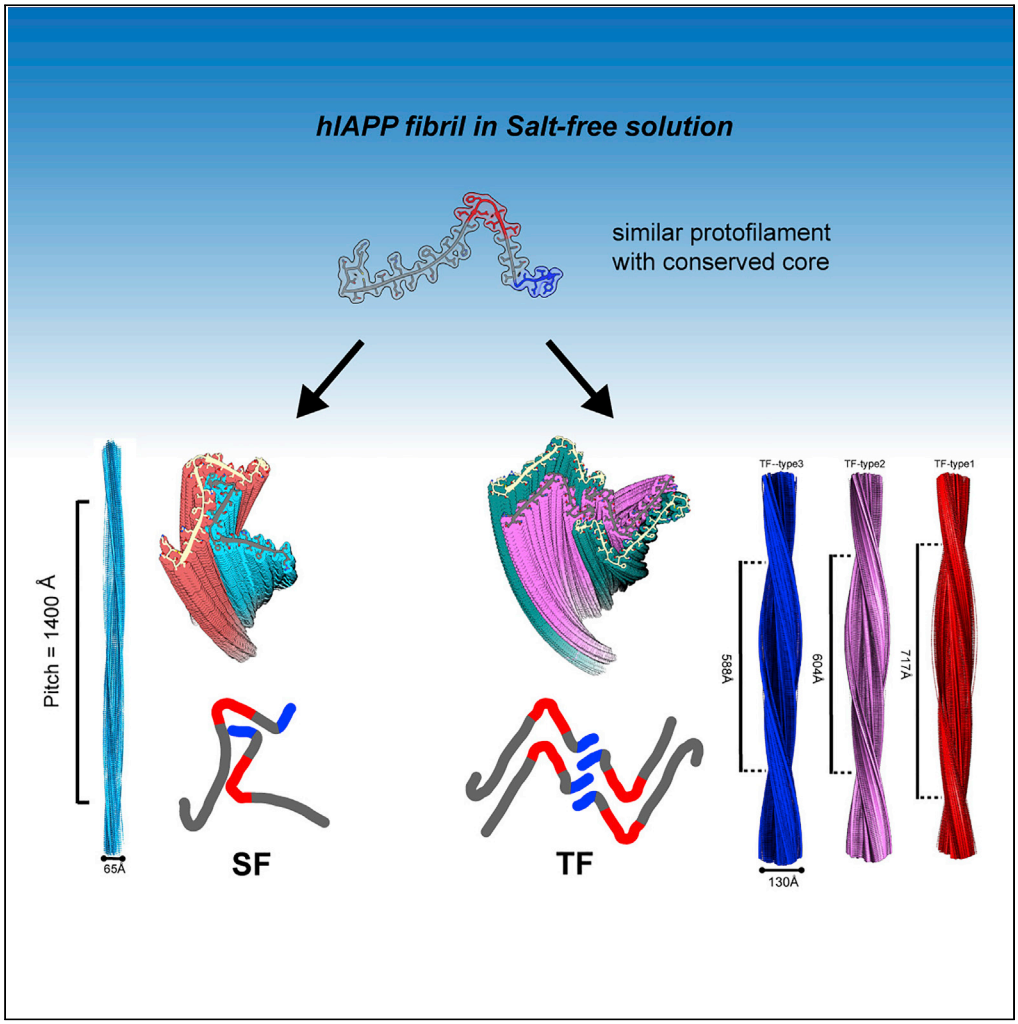

Dongyu Li, Xueli Zhang, Youwang Wang, Haonan Zhang, Kai Song, Keyan Bao, Ping Zhu

zhup@ibp.ac.cn

Highlights

Full-length cryo-EM structures of hIAPP fibrils in a salt-free environment

New polymorphic hIAPP fibrils with similar protofilaments but different interfaces

Different structures reveal a dynamic cross-over of hIAPP fibrils

Electrostatic interactions facilitate hIAPP fibril formation in salt-free solution

Li et al., iScience 25, 105705
December 22, 2022
https://doi.org/10.1016/j.isci.2022.105705

iScience

CellPress
OPEN ACCESS

Article

A new polymorphism of human amylin fibrils with similar protofilaments and a conserved core

Dongyu Li,[1,2,3] Xueli Zhang,[1,2,3] Youwang Wang,[1,2,3] Haonan Zhang,[1,2] Kai Song,[1] Keyan Bao,[1] and Ping Zhu[1,2,4,*]

SUMMARY

Pancreatic amyloid deposits composed of a fibrillar form of the human islet amyloid polypeptide (hIAPP) are the pathological hallmark of type 2 diabetes (T2D). Although various cryo-EM structures of polymorphic hIAPP fibrils were reported, the underlying polymorphic mechanism of hIAPP remains elusive. Meanwhile, the structure of hIAPP fibrils with all residues visible in the fibril core is not available. Here, we report the full-length structures of two different polymorphs of hIAPP fibrils, namely slim form (SF, dimer) and thick form (TF, tetramer), formed in a salt-free environment, which share a similar ζ-shaped protofilament but differ in inter-protofilament interfaces. In the absence of salt, electrostatic interactions were found to play a dominant role in stabilizing the fibril structure, suggesting an antagonistic effect between electrostatic and hydrophobic interactions in different salt concentrations environments. Our results shed light on understanding the mechanism of amyloid fibril polymorphism.

INTRODUCTION

Human islet amyloid polypeptide (hIAPP), also called amylin, is a 37-residue secretory hormone. As the major component of pancreatic amyloid deposits, hIAPP is cosynthesized and cosecreted with insulin by pancreatic islet β-cells[1–3] and is involved in multiple physiological processes, including glucose metabolism, energy homeostasis, gastric emptying, food intake, glucose homeostasis, and glucagon release.[4–6] However, under chronic hyperglycemic conditions associated with type 2 diabetes (T2D), overexpressed hIAPP aggregates into polymorphic protofilament forms, which can recruit and convert native hIAPP monomers into consistent or different fibril states to form amyloid deposits.[7,8]Aggregated hIAPP has been identified as a toxicant associated with the dysfunction and death of beta-cells, and found in over 95% of individuals with T2D.[4,9–12] The amyloidosis process of hIAPP and its toxicity are still not well understood.[13]

The polymorphic hIAPP fibril structural information is crucial to understanding hIAPP amyloid formation mechanisms and for the structure-based design of inhibitors of amyloidosis, which may provide insights for T2D treatments and other amyloid family diseases.[14–18] Recently, several high-resolution cryo-EM studies of hIAPP fibrils have provided critical insights into the polymorphic structures of hIAPP fibrils.[19–22] These studies revealed that different types of hIAPP peptides, e.g., synthetic hIAPP peptides[22] or recombinant SUMO-tagged hIAPP,[19] and variant growth conditions, e.g., TNI buffer,[19] MN buffer,[22] or seeded with patient-extract fibrils in PBS buffer[20] could form different types of conserved fibril cores and variant fibril architectures with distinct core interfaces and protofilament organizations. However, in contrast with the vast majority of polymorphic pathological fibrils such as tau and serum amyloid A (SAA) that possess very conserved protofilament and core morphologies,[23–26] the polymorphism of fibrils consisting of polymorphic protofilaments formed by hIAPP are not well understood.[27] Meanwhile, although both electrostatic interactions and hydrophobic interactions are considered critical for fibrillogenesis and fibril stabilization,[28] hIAPP can still form stable fibril morphologies and polymorphs in water that impedes hydrophobic interactions.[29] The mechanisms of hIAPP fibrillogenesis and polymorphism, e.g., where the polymorphs originate and how the structure of polymorphic protofilament influences the fibril architecture, remain to be studied.

In this study, we determined a set of high-resolution cryo-EM structures of hIAPP fibrils in a salt-free environment, i.e., reconstituted in water containing ~2% HFIP, with different polymorphic forms namely slim

[1]National Laboratory of Biomacromolecules, CAS Center for Excellence in Biomacromolecules, Institute of Biophysics, Chinese Academy of Sciences, Beijing 100101, China

[2]University of Chinese Academy of Sciences, Beijing 100049, China

[3]These authors contributed equally

[4]Lead contact

*Correspondence: zhup@ibp.ac.cn

https://doi.org/10.1016/j.isci.2022.105705

fibrils (SF, dimer) and thick fibrils (TF, tetramer) using helical reconstruction. Based on the cryo-EM density maps, we built an atomic model of the hIAPP protofilament with the full length of hIAPP peptide ($hIAPP_{1-37}$). Strikingly, the structural models reveal that the tetrameric thick fibril and dimeric slim fibril of hIAPP share an almost identical protofilament morphology but dramatically differ in inter-protofilament interactions. These structures indicate that hIAPP fibrils present a completely new polymorphism with a conserved protofilament but different organizations in the absence of salt, which suggests that the change of hydrophobic and electrostatic interactions in different salt conditions may affect the morphology and result in a different polymorphism of hIAPP fibrils. These data provide insights into the molecular mechanism of hIAPP fibril polymorphism.

RESULTS

hIAPP fibrillogenesis and polymorphism in different solutions

We synthesized a full-length hIAPP peptide (1-KCNTATCATQRLANFLVHSSNNFGAILSSTNVGSNTY-37) including an amidated C-terminus, prepared hIAPP amyloid fibrils by agitation in water with ~2% HFIP, i.e., a salt-free environment, and various buffers as reported in literature,[20,21] and then investigated the hIAPP fibrillogenesis kinetics and polymorphism by ThT binding assay. Apparently, fibrils grown in the water differ from those grown in the other buffer conditions in the growth kinetics (Figure 1A).[20,21] The ThT assay indicated that the growth rate was significantly accelerated in both PBS and ammonium acetate buffers compared with that in water. We hypothesized this may be attributed to the fact that PBS buffer contains 150 mM of salt ions. We then prepared hIAPP amyloid fibrils by agitation in solutions with different salt concentrations and performed similar ThT binding assays (Figure 1B). Not surprisingly, the hIAPP fibril grows much faster in the salty solutions than in that without salt, which is particularly remarkable in the physiological condition, i.e., 150 mM NaCl. These results suggest that hIAPP fibrillogenesis kinetics could be obviously influenced by the presence of salt in the solution. Although the fibril growth rate in salt-free environments that impedes hydrophobic interactions is much slower than that in salty solutions, the fibrils could still be readily observed.

We then applied negative-staining TEM to observe the fibrils grown in the absence and presence of salt with different concentrations (Figures 1C, 1D, and S1). Compared with the reported results,[19–22] hIAPP exhibits abundant new twig-like fibril morphologies without apparent twists under salt-free environments (Figure 1C). With the increase of the salt ions concentration in the solutions, the majority of fibrils exhibit a thicker rod form with twists (Figures 1 and S1). To explore whether the change of hydrophobic interactions will affect the architectures of mature fibrils, we changed the environment of fibrils pre-formed in solution without salt by adding variant amounts of salt ions to the solution and observed the architectures of resulting fibrils (Figures 1D and S2). NS-TEM results showed that the condensation of mature fibrils formed in absence of salt increased with the increase of salt ions concentration. A significant increase in the number of twisted fibrils was observed along with a decrease in the number of twig-like fibrils (Figure 1D). These results indicate that hydrophobic interactions, which become dominant as the electrostatic interactions get impeded with the addition of salt, will drastically accelerate the growth kinetics of the fibril and change the fibril morphology. Consequently, the hIAPP fibril in a salt-free environment with weaker hydrophobic interactions may be structurally different from the fibrils in a saline environment.

Structure determination of the hIAPP SF and TF fibrils

To determine the structures of hIAPP fibrils in a salt-free environment, we performed cryo-EM helical reconstructions in the hIAPP fibrils formed in water. Cryo-EM micrographs of the amyloid fibrils showed different and noteworthy fibrillar polymorphs, in which two dominant conformations were selected and subjected to further analysis (Figures 2A and S3 and Table 1). These two forms of fibrils include a thick form (named TF hereafter), and a slim form (named SF thereafter), occupying approximately 48% and 28% of the total particles, respectively (Figure 2B). The 2D classification showed obvious β-sheet separating along the fibril axis (Figures S4A and S4B). Using helical reconstruction in RELION3.0,[30] we acquired structures of dimeric SF with a width of 65 Å at a resolution of 3.6 Å (Figures 2C and S6A) and three representative forms of tetrameric TF fibrils by classification (TF-type 1\TF-type 2\TF-type 3) with maximum and minimum widths of 130 Å and 66 Å at resolutions of 3.3 Å, 3.2 Å, and 3.3 Å, respectively (Figures 2D, S5, and S6B). Although the reconstruction resolution is not sufficient to determine the handedness, a left-handed twist, which is common in amyloid fibrils, was assumed for both SF and TF fibrils. The dimeric SF fibril is composed of two protofilaments intertwining along an axis with a helical rise of 4.76 Å and a helical twist of −1.22°, whereas the three types of classified tetrameric TF fibrils consist of 4 intertwined protofilaments with a

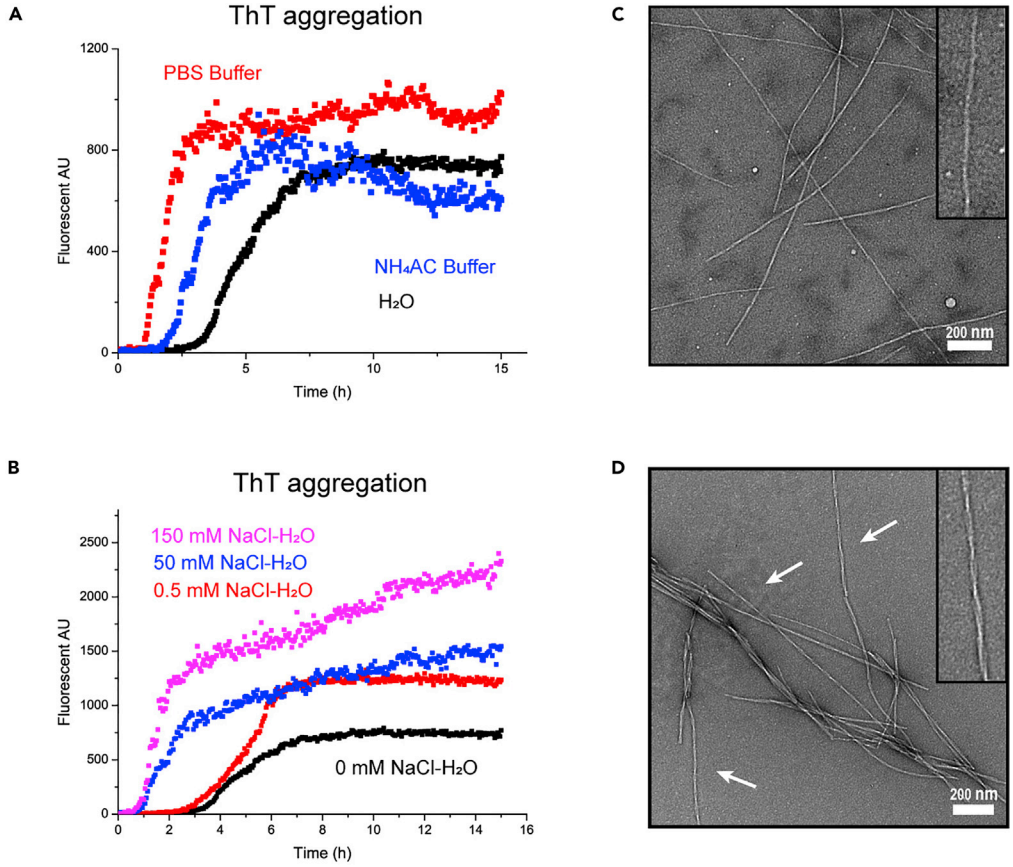

Figure 1. Biochemical characterization and negative stain EM of hIAPP in different solvent environments

(A) ThT assay measuring kinetics of hIAPP agitation in different buffer solutions: water (black), PBS buffer (red), NH4AC buffer (blue).

(B) ThT assay measuring kinetics of hIAPP agitation in different salt concentrations: 0 mM (black), 0.5 mM (red), 50 mM (blue), 150 mM (magenta).

(C) Negative-stain EM of hIAPP fibril in water. Twig-like fibril is evenly distributed across the carbon film.

(D) Negative-stain EM of mature hIAPP in water followed by the adding of 100 mM NaCl. The twisted fibrils are clustered on the carbon film. The white arrow indicates the twisted shape of the fibrils. The black box in the upper right corner in (C) and (D) shows an enlarged view of the typical fibril in their solution. Scale bar 200 nm.

pseudo-2-fold symmetry and a consistent helical rise of 2.35 Å but three different helical twists of 179.28°, 179.30° and 179.41°, respectively. Based on the 3D classification and reconstruction results, we found that the TF fibrils contained a variety of fibril types with similar morphologies but different helical forms (Figures 2D and S5). Having the best final reconstruction resolution, TF-type 2 was chosen as the representative canonical fibril for structural analysis with SF, whereas the other two classes of fibrils were described later. Based on the cryo-EM maps, we built atomic models of the full-length hIAPP peptide in one of the two asymmetric monomers of SF and TF fibrils and atomic models of hIAPP regions, including R11-Y37 and T9-Y37, in the other asymmetric monomers of SF and TF fibrils (Figures 2C and 2D). Approximately 26% of the total particles, which show morphologies with larger heterogeneity and different pitches in the 2D class averages, were not well defined at high resolution (Figure 2B). To be worthy of note, the N-terminus of TF fibril also shows a high similarity to that in a previously reported structure (Figure S6E).[20]

The cross-seeding between hIAPP and amyloid-β fibrils in patients may relate to the clinical link between T2D and Alzheimer's disease.[31–35] Previous electron microscopy studies have shown a similar S-typed protofilament in both hIAPP and Aβ(1–42) fibrils.[22] At the same time, this form of fibril has been found ubiquitous in different growth buffer environments.[20–22] Of interest, in addition to the dominant TF and SF architectures, other identifiable morphologies, e.g., two S-like shaped intertwined protofilaments with pseudo

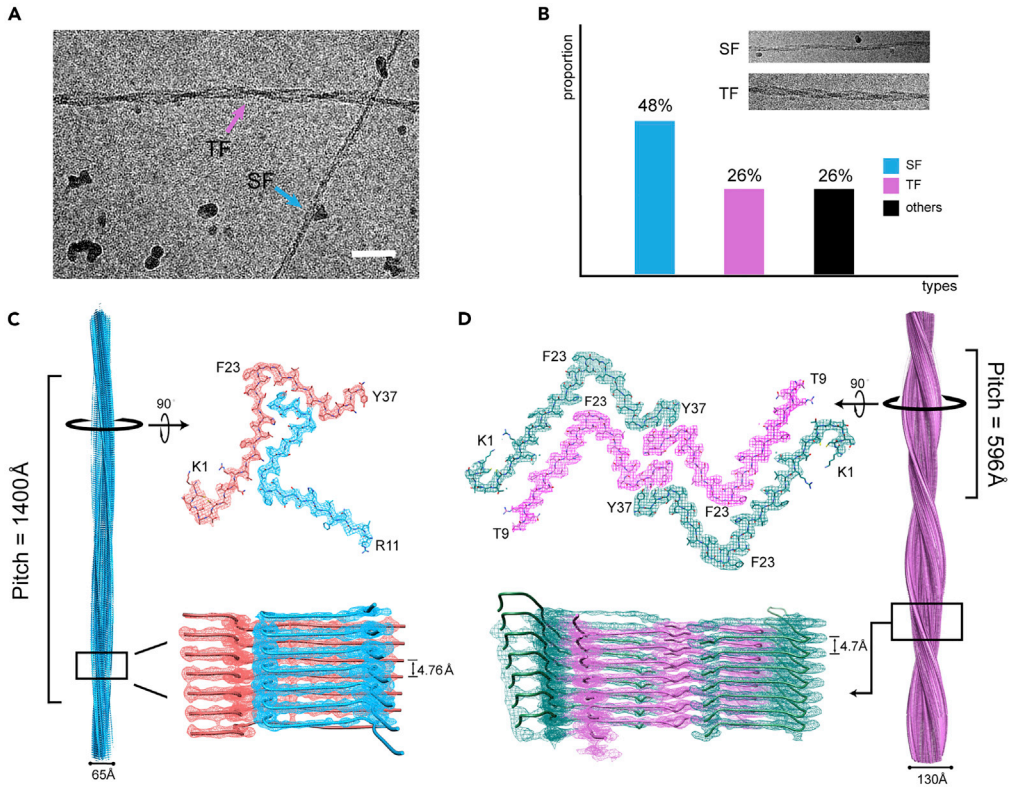

Figure 2. Cryo-EM structures of hIAPP polymorphs

(A) Representative cryo-EM micrograph indicating fibril polymorph1 (SF, dodger blue arrow) and polymorph 2 (TF, orchid arrow), bar 40 nm.

(B) Raw cryo-EM images and proportions of major polymorphs: SF (dodger blue) and TF (orchid) fibril.

(C and D) Cryo-EM structures of the SF and TF polymorphs of the full-length hIAPP fibrils superimposed with atomic models shown in different views. The 3D maps of the SF and TF fibril polymorphs are shown on the left and right panel, respectively, with their distinctively different helical pitches depicted. Four kind protofilaments are colored by blue and red for SF, orchid and teal for TF, respectively. The distance between neighboring subunits in one protofilament is indicated.

symmetry that appear similar to the shapes reported previously,[20–22] were also acquired by averaging parts of the particles within the 26% portion (Figures S3D and S4C). Strikingly, a ζ-shaped Aβ monomer structure, which is similar to the ζ-shaped hIAPP monomer structure revealed in this study, had also been reported to exist in a salt-free environment in a previous study (Figure S10).[36] The existence of similar ζ-shaped monomeric hIAPP and Aβ fibrils may indicate that Aβ and hIAPP have a similar polymorphic mechanism in the salt-free environment. This result provides a structural basis for the cross-seeding of Aβ and hIAPP in different environments.

SF and TF shared similar ζ-shaped protofilaments with a common kernel

Strikingly, although the dimeric SF and tetrameric TF fibrils display different architectures, the secondary structure arrangements of the SF and TF monomers show a similar shape, i.e., a ζ-motif (Figures 3A and 3B). For clarification, we named the two protofilaments in SF D-1 (K1-Y37, SF) and D-2 (R11-Y37, SF), and the protofilaments in TF with pseudo-2_1 symmetry T-1 (K1-Y37, TF-type 2), T-2 (T9-Y37, TF-type 2), T-1′ and T-2′, respectively. Each ζ-shaped monomer consists of three β-sheets, namely, β1 (A8-N22), β2 (I26-N31), and β3 (N35-Y37), which are linked by three turns, namely, turn A (T4-T6), turn B (F23-A25) and turn C (V32-S34), respectively (Figures 3A, 3B, and S7). In both monomers with full-length structures solved in SF and TF, i.e., D-1 and T-1, disulfide bonds between C2 and C7 were clearly identified (Figures 3C, 3D, and S6D). For the dimeric SF fibril, the N21-S29 core regions of D-1 and D-2 monomers maintained tremendous consistency with a root-mean-square deviation (RMSD) of 0.1 Å for the Cα atoms (Figure 3C). The angles of turn B within the core region of D-1 and D-2 are almost the same, with a value of 60°, but the angle of

Table 1. Cryo-EM data collection, refinement and validation statistics

	#1 SF (EMDB-33897)(PDB 7YKW)	#2 TF-type1 (EMDB-33902) (PDB 7YL3)	#3 TF-type2 (EMDB-33901) (PDB 7YL0)	#4 TF-type3 (EMDB-33903) (PDB 7YL7)
Data collection and processing				
Magnification	130,000	130,000	130,000	130,000
Voltage (kV)	300	300	300	300
Electron exposure (e–/Å^2)	1.87	1.87	1.87	1.87
Defocus range (μm)	1.5to2	1.5to2	1.5to2	1.5to2
Pixel size (Å)	1.04	1.04	1.04	1.04
Symmetry imposed	C1	2^1	2^1	2^1
Helical rise (Å)	4.76	2.35	2.35	2.35
Helical twist (°)	−1.22	179.28	179.30	179.41
Initial particle images (no.)	165,845	89,123	89,123	89,123
Final particle images (no.)	58,039	28,593	29,512	29,587
Map resolution (Å)	3.6	3.3	3.2	3.3
FSC threshold	0.143	0.143	0.143	0.143
Map resolution range (Å)	200–3.6	200–3.3	200–3.2	200–3.3
Refinement				
Initial model used (PDB code)	*De novo*	*De novo*	*De novo*	*De novo*
Map sharpening *B* factor (Å^2)	−100	−73	−73	−71
Model composition				
Non-hydrogen atoms	1908	2958	2958	2988
Protein residues	256	396	396	402
Ligands	0	0	0	0
B factors (Å^2)				
Protein	85	108	104	108
Ligand	–	–	–	–
R.M.S. deviations				
Bond lengths (Å)	0.009	0.008	0.014	0.009
Bond angles (°)	1.581	2.235	2.372	0.960
Validation				
MolProbity score	1.81	2.04	2.12	2.18
Clashscore	10.73	21.81	18.86	22.05
Poor rotamers (%)	0	0	0	0
Ramachandran plot				
Favored (%)	96.12	96.67	95	95.08
Allowed (%)	3.88	3.33	5	4.92
Disallowed (%)	0	0	0	0

turn C of D-1 (78°) is larger than that of D-2 (54°) (Figures 3C(i) and 3C (ii)). Moreover, the β1 region of D-1 is inwardly curved compared with that of D-2. Similarly, in the tetrameric TF fibril, T-1 and T-2 monomers also maintain a high consistency at turn B (61°) and present different bending angles at turn C (T1: 74°, T-2: 89°), whereas the N21-S28 core regions are conserved with a Cα RMSD of 0.35 Å (Figures 3D(i) and 3D(ii)). Of interest, the alignment of all four protofilaments in the TF and SF fibrils shows that they share a common kernel region, i.e., 21-NNFGAILSS-29, which presents a highly conserved conformation among the four protofilaments, although the N-terminus and C-terminus display some flexibility and variation (Figure 3E).

Previous studies have suggested that the amino acid ladder formed along the helical axis, such as aliphatic or aromatic residues, asparagine, and glutamine side chain stacks, can increase the fibril stability of amyloid

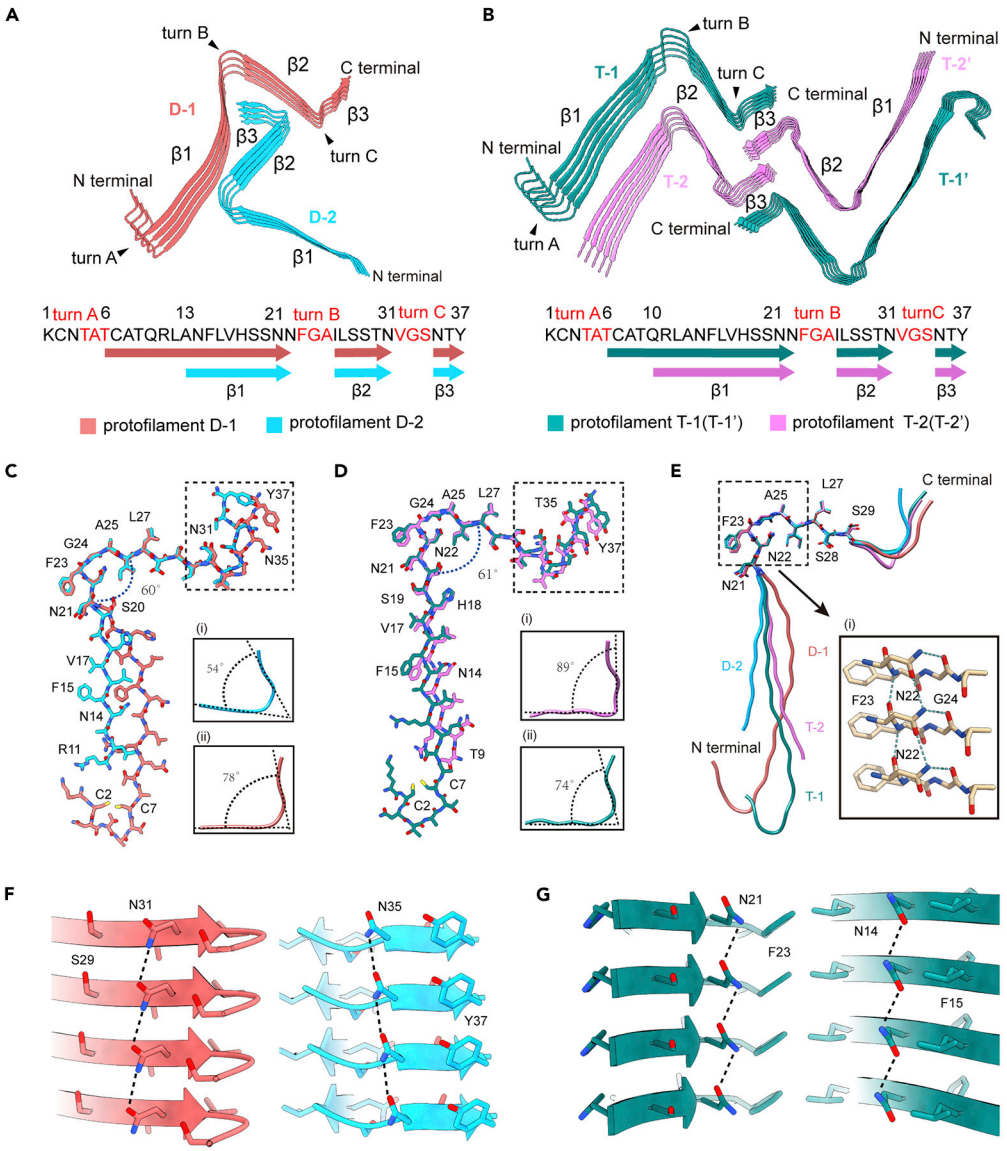

Figure 3. The similar architectures of protofilaments in SF and TF

(A and B) Rendered view of the secondary structure of SF fibril and TF fibril contain four type protofilaments: D-1 (red), D-2 (blue), T-1 (teal), T-2 (orchid). Three β-strands (β1, β2 and β3) and three turns (turn A, turn B and turn C) in one hIAPP monomer are indicated in sequential and schematic view under panel.

(C) Superposition of the two-type monomers in SF fibrils. Two-type ζ-shaped monomers show a coincident angle 60° in turn B (N21-I26). The angles of turn C at the C-terminus of monomer D-2 and D-1 are magnified in (i) and (ii) respectively.

(D) Superposition of the monomers in TF fibrils, which shows a coincident angle 61° in turn B (N21-I26). The angles of turn C at the C-terminus of monomer T-2 and T-1 are magnified in (i) and (ii) respectively.

(E) An overlay of four type monomers of the SF and TF polymorphs reveals a similarity of protofilaments. Intra-protofilament hydrogen bond ladders formed between N22 and G24 at turn B are magnified in (i).

(F) Asparagine ladders (N14s, N21s, N31s, N35s) of protofilament D-2 and D-1 stabilizes the SF fibril N14s and N21s are chosen to show.

(G) Stacking of aromatic side chains and asparagine ladders (N14s, N21s, N31s, N35s) in protofilament T-1 stabilizes the TF fibril. N31s and N35s are chosen to show.

fibrils. In addition, the buried polarity ladder tends to interact with each other, which may be responsible for the formation of hydrogen bonding networks.[28] Consistent with these data, the contribution to the hydrogen bonding network from hydrogen bonds between N22's side chain amino group and G24's

main chain carboxyl group and the polar ladder alongside the fibril axis formed by N22 was found to play an important role in maintaining the stabilization of turn B in the core region (Figure 3E(i)). However, different from turn B, N31s and G33s in turn C present only hydrogen bonds between side chains, suggesting that the structure of turn C is more flexible than that of turn B. In addition to the hydrogen bond network in turn B, other interactions could also help to stabilize the fibril architectures, including aromatic amino acid (F15, F23, Y37) ladders in all protofilaments, hydrogen bond ladders formed by Asparagine residues (N14, N21, N31, N35) in which those of N31s and N35s appear more apparent in SF fibrils (Figure 3F) and those of N14s and N21s are more obvious in TF fibrils according to densities (Figure 3G).

SF and TF adopt different interaction modes among the protofilaments

Although the protofilaments of SF and TF share a similar ζ shape, the lateral contacts and interaction modes between the two protofilaments of SF and TF are distinctly different (Figure 4). For SF, the A25-S29 fragment of D-2 interplays with the A13-V18 fragment of D-1 in a zipper pattern (Figure 4A(i)), in which the hydrogen bond ladder formed by D-2 N14 with D-1 A25 helps to stabilize the fibril (Figure 4A(ii)). In addition, the C-terminus (G33-Y37) of D-2 interacts with the turn B I26-N31 fragment of D-1 in a wedge mode, resulting in two hydrogen bonds between D-2 Y37 and D-1 S28, D-2 G33, and D-1 T30 (Figures 4A(iii) and 4A(iv)). The β lamellae between the two protofilaments are staggered, and layer i of D-1 is located between layer j and layer j+1 of D-2 (Figure S8A). These interfaces may reduce the flexibility of turn C of D-2 so that it cannot stretch out like the C terminus of D-1 and stabilize the β1 region of D-1. For TF, the cross-section of four protofilaments, which interlace with each other at the β3 region of the C-terminus, exhibits a symmetric pattern, resulting in four symmetric hydrogen bonds between N35 and Y37 (Figures 4B(i) and 4B(iii)). The longer steric zipper interface between fragment T9-H18 in β1 of T-2 and fragment L12-S20 in β1 of T-1 helps to stabilize the N-terminal regions of the TFs (Figure 4B(ii)). The β lamellae between the two TF protofilaments are also staggered, whereas layer j of T-2 is located between layer i and layer i-1 of T-1′ (Figure S8B). Due to the large torsion state of the TF, T-1 decreases from the N-terminus to the C-terminus along the z axis direction with 10.5° and 10 Å, whereas T-2 decreases from N-terminus to the C-terminus along the z axis direction with 5.5° and 4 Å. In addition, layer j of T-2 rises from layer i-2 to layer i of T-1 in the inter-protofilament interface (Figures S8C and S8E). Our structures suggest that the interplays between protofilaments that are dominated by electrostatic interactions play a critical role in stabilizing the fibril structures in a salt-free solution.

Although impeded under salt-free environments, hydrophobic interactions still play their roles in stabilizing the fibril structures. Our structures show that the interfaces of hIAPP fibrils are composed of only parts of hydrophobic residues. In SF, the hydrophobic region consists of A25, L27, and Y37 of D-2, together with L12, L16, and I26 of D-1 (Figures 4A and S9A), whereas in TF, the hydrophobic region is relatively dispersed, consisting of residues A13, F15, V17, A25 and L27 of T-2 along with A8, L12 and V32 of T-1 (Figures 4B and S9B). Of interest, in our cryo-EM maps, certain hydrophobic residues were exposed instead of being buried inside the protein, e.g., A5, A8, A13, F15, and V17 of D-1, A13, F15, V17, and V32 of D-2, A13, F15, and V17 of T-1, and L12, L16, I26 and V32 of T-2. However, some extra density islands were observed surrounding the exposed hydrophobic residues, which are most likely contributed by other protofilaments to help maintain the stability of the fibril by burying hydrophobic residues inside (Figures S9C and S9D).

In the absence of salt, the hydrophobic and electrostatic interactions are different among the protofilaments with variant morphologies, e.g., SF and TF. Furthermore, the different hydrophobic and electrostatic interactions between the protofilaments can also slightly change the protofilaments' architecture, although they still share an overall common ζ-shape. In SF, the hydrophobic cross-section and the hydrogen bond network formed by residues A25 (D-1) and N14 (D-2) result in the curved β1 region in D-1 (Figure 4A(ii)). In TF, the β1 regions in T-1 and T-2 are relatively flat and parallel owing to the homodisperse hydrophobic residues. In addition, a longer steric zipper in the β1 region of TF contributes to the stabilization of the N-terminus compared with the flexible N-terminus of SF.

Dynamically changing helical states in TF

Fibril formation is a dynamic process. The instability of crossover had been thought to be a manifestation of fibril polymorphism. In our study, the heterogeneous crossover of the TFs was observed, ranging from 550 Å to 800 Å (Figure 5A). Among these heterogeneous fibrils, three types of high-resolution TF structures with different compaction rates as described by accurate helical pitches of 588 Å (type-1), 604 Å (type-2), and 717 Å (type-3) were obtained by helical reconstruction. Structural analysis/classification revealed

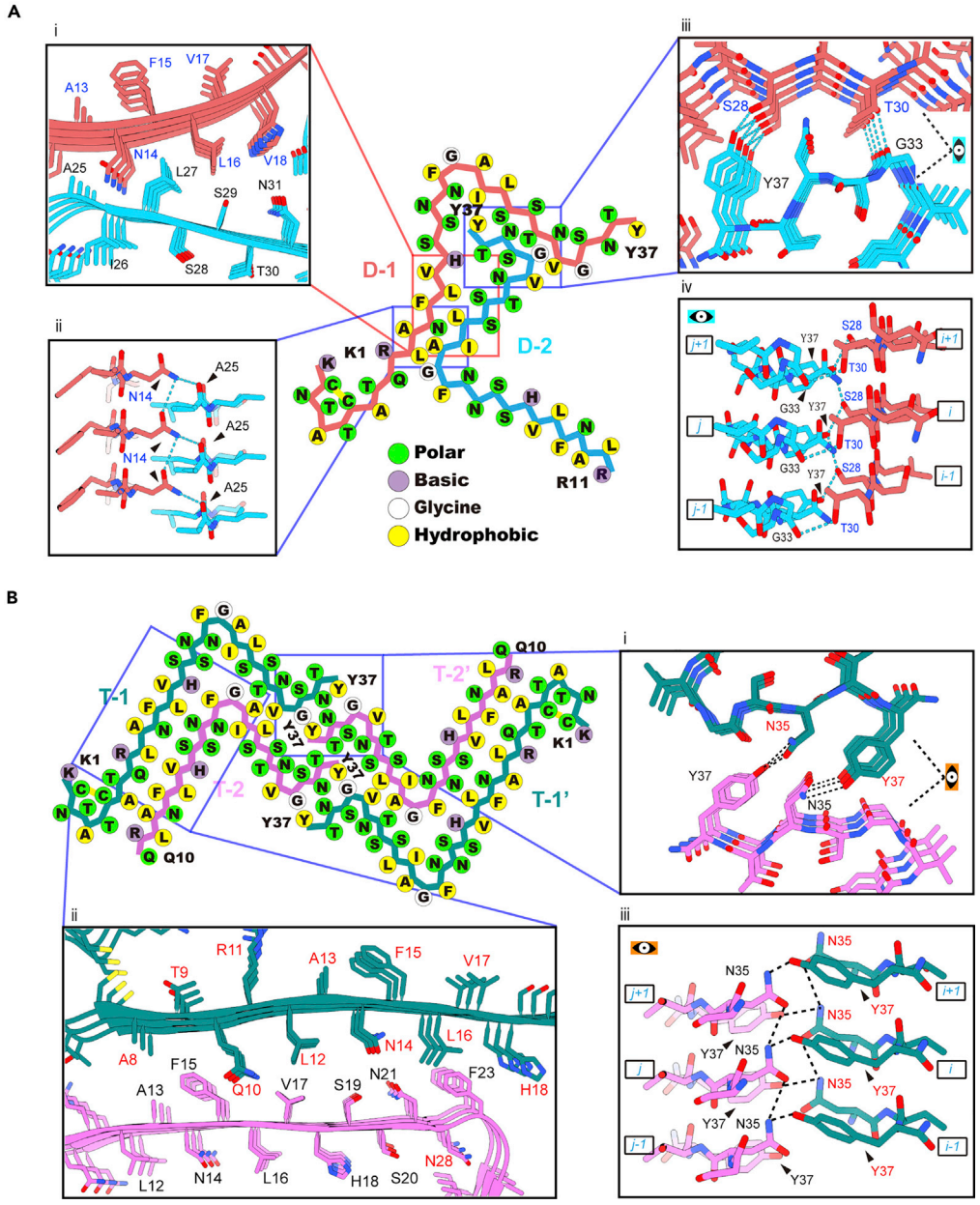

Figure 4. The distinct interface in SF and TF fibril structures

(A) Schematic view of SF fibril. The backbones are colored by protofilament, as in Figure 1C. (i), (iii) interfaces between protofilament D-1 and D-2 packed steric zippers of SF fibril. (ii) side-chain H-bonds interactions across the inter-protofilament interface between N14 of D-1 and A25 of D-2. (iii), (iv) H-bonds across the inter-protofilament interface between G33, Y37of D-2 and T30, S28 of D-1, zig-zagging up and down the interface.

(B) Schematic view of each monomer for TF fibril. The backbones are colored by protofilament, as in Figure 1C. (i), (ii), Interfaces between T-1(T-1′) and T-2′(T-2) packed steric zippers of TF fibril. (i), (iii) side-chain interactions consistent with H-bonds ladder across the inter-protofilament interface between N35, Y37 of T-1 (T-1′) and Y37, N35 of T-2′(T-2).

that these three types have almost equal percentages in the total picked particles (type-1: 33%, type-2: 32%, type-3: 33%) (Figure 5B). From the loose helical state (type-1) to the tight helical state (type-3), the overall morphologies and the interaction modes between the protofilaments were basically unchanged (Figure 5C). However, when comparing the three forms of T-1 protofilaments, the main chains of the N-terminus were found highly consistent before I26 by keeping the N-terminus aligned, whereas the

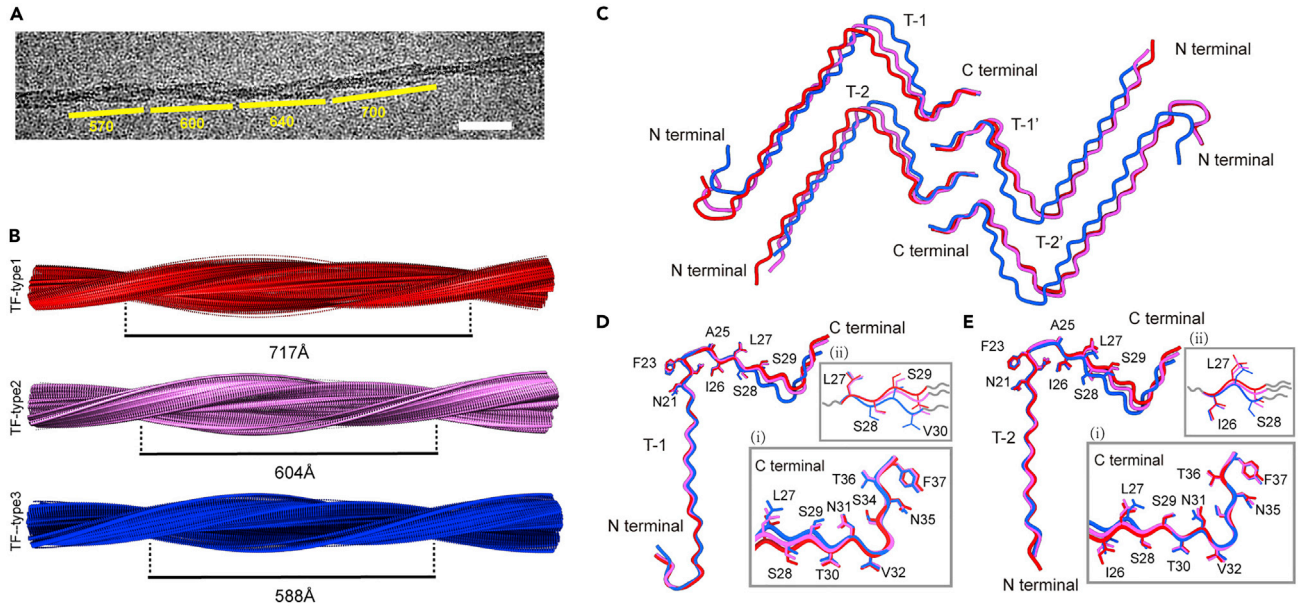

Figure 5. Dynamic helical pitch in TF fibril

(A) Raw cryo-EM image shows a TF fibril with dynamic helical pitch, bar 40 nm.

(B) Superposition of the three types TF fibril models: type 1 (red), type 2 (orchid), type 3 (blue).

(C) Reconstructed of three types WFs fibrils with different helical pitches. Dust arrows indicate the monomer changing directions in different fibrils.

(D) Superposition of the protofilament T-1 monomers in three TF polymorphs based on the alignment of N terminal. (1) Superposition of the C terminal of protofilament T-1 monomers in three TF polymorphs. (2) The peptide backbone is changed at L27-V30.

(E) Superposition of the protofilament T-2 monomers in three TF polymorphs based on the alignment of N terminal. (1) Superposition of the C terminal of protofilament T-2 monomers in three TF polymorphs. (2) The peptide backbone is changed at I26-S28.

main chains of the C-terminus were highly consistent after S28 by keeping the C-terminus aligned. This observation indicates that deformation of the monomer may occur in the region I26-S28 (Figures 5D(i) and 5D(ii)). A similar analysis of monomer T-2 suggested that deformation may occur between L27 and V30 (Figures 5E(i) and 5E(ii)). These results indicate that the β2 region of hIAPP tends to be more flexible than other regions.

DISCUSSION

Electrostatic and hydrophobic interactions involved in hIAPP fibrillation and polymorphism

Previous studies of polymorphic hIAPP fibrils formed with saline solution *in vitro* and seeded from patient tissue extraction illustrated the protofilaments polymorphism.[19–22] Among them, it has been pointed out that polymorphic hIAPP fibrils and protofilaments have multiple conserved cores.[20] In contrast, our polymorphic fibril structures formed in a salt-free environment possess a similar protofilament morphology and one single conserved core (21-NNFGAILSS-29). By comparing the structure of ζ-shaped protofilament with other hIAPP protofilament structures solved under different conditions, very different architectures of protofilaments including the core regions, are noticeable, although some of them present a similar core region structure (N21-L27) (Figure S11). Hydrophobic and electrostatic interactions are the basis for maintaining fibril structure.[28] When the concentration of salt ions in solution changes, the hydrophobic and electrostatic interactions will change accordingly. That is, the hydrophobic interactions get strengthened and the electrostatic interactions get weakened when the salt ion concentration increases, whereas the opposite effect occurs when the salt ion concentration decreases. So, for the difference in protofilament structures under different saline conditions, we speculate that this may be related to the antagonism of electrostatic interactions and hydrophobic interactions within the hIAPP fibril under various growth environments with different salt concentrations.

Of interest, apart from polymorphism, the growth kinetic properties of hIAPP fibrils also displayed different in salt-free and salt-containing solutions. Our results show a highly promoting effect of salt

concentration on hIAPP fibril growth rate and ThT intensity (Figures 1A and 1B). These indicate that the hydrophobic interaction-based fibrillation process is vigorous and rapid in a high-salt environment. On the other hand, the fibrillation process is relatively mild in the salt-free environment. This differential fibril growth kinetics phenomenon could be related to a similar factor which leads to the different fibril polymorphs. Strong hydrophobic interactions in a high-salt environment are more conducive to hIAPP fibrillation formation, resulting in polymorphic fibrillar structures. The fibrillation process driven by electrostatic interaction in water is gentler and smoother, which helps to form a relatively uniform fibril structure. When salt ions are introduced into water, the original mature fibril structures in water are affected, due to the weakening of the electrostatic interaction and the enhancing of the hydrophobic interaction This further explains the change of fibril morphology when salt was added to the water as we observed with negative staining EM (Figures 1D and S2A–S2D). Of interest, a "reversed" packing condensation of protofilaments could be observed with the "removal" of salt (Figures S2E and S2F). The morphology and twist of fibrils formed in the presence of salt also changed slightly with the removing of salt, but less than that of adding salt (Figure S2). It is worth noting, however, the removal of salt from the salt solution in the widely used fibril ice-water extraction method[37] appears to have a limited effect on the fibril structure. The underlying mechanism of this differentiation phenomenon is still worth exploring, for example, whether the protofilament could change the morphology from the ζ shape in salt-free environment to S shape in saline solution, which needs high resolution structures formed in different conditions.

A polymorphism model of hIAPP amyloid

In this study, we elucidate the growth kinetics and morphological changes of hIAPP fibrils in different solutions (Figures 1, S1, and S2), and reported two different hIAPP fibril structures with conserved ζ-shaped protofilaments, SF and TF under a salt-free environment (Figure 2). The three β sheets linked by three turns in the protofilament structures are analogous to the previously reported results from crystallographic and NMR studies (Figures 3A, 3B, and S7). In each hIAPP protofilament of SF and TF, turn B located at the core region 21-NNFGAILSS-29 is extremely conserve (Figure 3E). However, the angles of turn C at the C-terminus of the four types of protofilaments are more variable compared with those of turn B, which differ with the binding patterns and cause the fibril to present a diverse state. This may be attributed to the fact that the C-terminal region (33-GSNTY-37) in one protofilament interacts with the other protofilaments at two different action sites (Figures 4A(iii) and 4B(i)), leading to various fibril morphologies, e.g., SF and TF. The calculated interface areas of the two types of fibrils are in the same range (SF: 2880 $Å^2$, TF: 2903 $Å^2$), which suggests that these two forms of fibrils are comparable in terms of structural stability.

Our structures suggest a model of polymorphism that hIAPP fibrils in a salt-free environment are composed of similar protofilaments (Figures 6A and6B),[38] which interact in different ways leading to various fibril morphologies, e.g., SF and TF (Figure 6C). With this block-building pattern, other fibril polymorphic architectures could also be speculated (Figure 6D). In the salt-free environment, electrostatic interactions play a dominant role in the hIAPP fibril cross-section morphological structure. For the fibrils in the salt solution, in addition to the polymorphic fibril structure, the interaction interface is very different, too. Noticeably, all different structures in the salt solutions suggest that the fibrils try to embed the hydrophobic amino acid residues inside and isolate them from the solvent. This indicates that hydrophobic interactions play a dominant role in forming different hydrophobic cores and hydrophobic interfaces in the salt solution. Meanwhile, in the presence of salt, the electrostatic interactions maintaining the conserved core is getting weakened, whereas the hydrophobic interactions get strengthened, which result in a structural change in the conserved core region to embed the hydrophobic residues thus forming polymorphic protofilaments and fibril structures (Figures 6A, 6E and6F). Of interest, our structure of hIAPP solved in the absence of salt shows an almost identical shape to that of the crystal structure of hIAPP (N21-L27) in the core region, indicating that fibrils are highly conserved in the core region without the influence of other hydrophobic amino acids outside the core region (Figure S12).[39] Therefore, the antagonistic effect of hydrophobic and electrostatic interactions with the change of salt ion concentration in solution may play an important role in affecting the growth and morphology of hIAPP fibrils. In summary, we have determined the cryo-EM structures of two full-length hIAPP fibrils with similar protofilament compositions stabilized by electrostatic interactions in a salt-free environment. The protofilaments of two hIAPP fibrils are highly conserved in the core region of 21-NNFGAILSS-29 and form distinct architectures through different interactions with the C-terminus. The new ζ-shaped protofilaments and

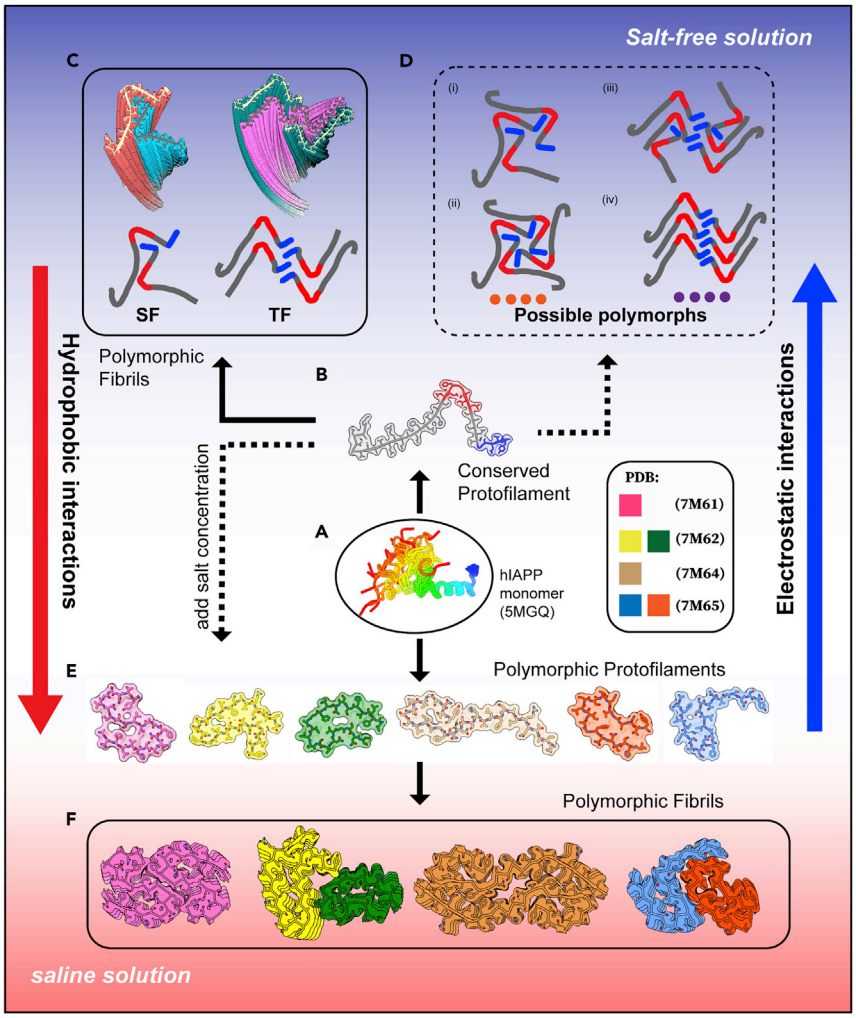

Figure 6. A polymorphism model of hIAPP amyloid in hypotonic and hypertonic solution

(A) The hIAPP monomers.

(B) Protofilament formed from the monomer with stable core region (red) and activate C terminus (blue).

(C) Dimer or tetramer fibrils assembled with similar ζ-shaped protofilament and different interaction modes in salt-free solution.

(D) Based on the interaction modes, dotted line from (B) to (D) indicated that other possible fibril forms can be inferred: (1) Trimer and (2) tetramer formed by SF interactive model, (3) hexamer fibril formed by TF and SF interactive model and (4) TF interactive model.

(E) When hIAPP is in hypersaline solution, the monomer could form polymorphic protofilaments under the influence of hydrophobic interaction. Dotted line from (B) to (E) indicated the uncertain fibrillary morphology changes when the solution environment changes from salt-free to hypersaline.

(F) Polymorphic fibril formed with different morphologies formed from polymorphic protofilaments.

interaction patterns of hIAPP fibrils in a salt-free environment indicate a distinct mechanism of fibril polymorphism, in contrast with those amyloid fibrils grown in salt solutions. The result, combined with the previous studies, elucidates that the unique polymorphism of hIAPP fibril could be regulated by electrostatic interactions and hydrophobic interactions.

Limitations of the study

This study shows a new architecture of hIAPP fibrils with similar protofilaments and a conserved core in a salt-free environment, which suggests a distinct polymorphism of human amylin fibrils. However, the biological relevance of this polymorphism is still worth exploring owing to the facts that salt-free environment

is hard to identify in cells. Besides, the high resolution cryo-EM structures and the reversibility of fibrils in different environments is worth investigating.

STAR★METHODS

Detailed methods are provided in the online version of this paper and include the following:

- KEY RESOURCES TABLE
- RESOURCE AVAILABILITY
  - Lead contact
  - Materials availability
  - Data and code availability
- METHOD DETAILS
  - Sample preparation of hIAPP$_{1-37}$ amyloid
  - Thioflavin T (ThT) binding assay
  - Effect of salt concentration on mature fibril morphology
  - Negative-stain EM analysis of hIAPP amyloids
  - Cryo-electron microscopy sample preparation of hIAPP amyloids
  - Helical reconstruction
  - Model building and refinement
- QUANTIFICATION AND STATISTICAL ANALYSIS

SUPPLEMENTAL INFORMATION

Supplemental information can be found online at https://doi.org/10.1016/j.isci.2022.105705.

ACKNOWLEDGMENTS

This work was supported by grants from the Chinese Ministry of Science and Technology (2017YFA0504700, 2018YFE0203300, 2021YFA1300100), the National Natural Science Foundation of China (31730023, 31521002), and the Chinese Academy of Sciences (CAS) (XDB37010100). Cryo-EM data collection in this work was carried out at the Center for Biological Imaging, Core Facilities for Protein Science at the Institute of Biophysics (IBP), Chinese Academy of Sciences (CAS). We thank Xiaojun Huang, Boling Zhu, Xujing Li, Gang Ji, and other staff members at the Center for Biological Imaging (IBP, CAS) for their support in data collection. We thank Prof. Chen Wang at National Center for Nanoscience and Technology (NCNST), China, for his insightful discussion and critical comments on the project and manuscript.

AUTHOR CONTRIBUTIONS

P.Z. conceived the study. X.Z. prepared hIAPP fibrils and cryo-EM samples, and performed cryo-EM data collection. D.L. and H.Z. performed data processing and analysis. X.Z. and Y.W. built and refined the structural models. D.L., Y.W., X.Z., and P.Z. analyzed the results. D.L, Y.W., and P.Z. wrote the manuscript. All authors discussed and commented on the results and the manuscript.

DECLARATION OF INTERESTS

The authors declare no competing interests.

Received: August 22, 2022
Revised: October 7, 2022
Accepted: November 29, 2022
Published: December 22, 2022

REFERENCES

1. Lukinius, A., Wilander, E., Westermark, G.T., Engström, U., and Westermark, P. (1989). Co-localization of islet amyloid polypeptide and insulin in the B cell secretory granules of the human pancreatic islets. Diabetologia *32*, 240–244.
2. Kahn, S.E., D'Alessio, D.A., Schwartz, M.W., Fujimoto, W.Y., Ensinck, J.W., Taborsky, G.J., Jr., and Porte, D., Jr. (1990). Evidence of cosecretion of islet amyloid polypeptide and insulin by β-cells. Diabetes *39*, 634–638.
3. Stridsberg, M., Sandler, S., and Wilander, E. (1993). Cosecretion of islet amyloid polypeptide (IAPP) and insulin from isolated rat pancreatic islets following stimulation or inhibition of beta-cell function. Regul. Pept. *45*, 363–370.

4. Westermark, P., Andersson, A., and Westermark, G.T. (2011). Islet amyloid polypeptide, islet amyloid, and diabetes mellitus. Physiol. Rev. *91*, 795–826.

5. Lutz, T.A. (2010). The role of amylin in the control of energy homeostasis. Am. J. Physiol. Regul. Integr. Comp. Physiol. *298*, 1475–1484.

6. Montane, J., Klimek-Abercrombie, A., Potter, K.J., Westwell-Roper, C., and Bruce Verchere, C. (2012). Metabolic stress, IAPP and islet amyloid. Diabetes Obes. Metab. *14*, 68–77.

7. Goldsbury, C.S., Cooper, G.J., Goldie, K.N., Müller, S.A., Saafi, E.L., Gruijters, W.T., Misur, M.P., Engel, A., Aebi, U., and Kistler, J. (1997). Polymorphic fibrillar assembly of human amylin. J. Struct. Biol. *119*, 17–27.

8. Wineman-Fisher, V., and Miller, Y. (2016). Structural insights into the polymorphism of self-assembled amylin oligomers. Isr. J. Chem. *56*, 590–598.

9. Jurgens, C.A., Toukatly, M.N., Fligner, C.L., Udayasankar, J., Subramanian, S.L., Zraika, S., Aston-Mourney, K., Carr, D.B., Westermark, P., Westermark, G.T., et al. (2011). β-cell loss and β-cell apoptosis in human type 2 diabetes are related to islet amyloid deposition. Am. J. Pathol. *178*, 2632–2640.

10. Akter, R., Cao, P., Noor, H., Ridgway, Z., Tu, L.H., Wang, H., Wong, A.G., Zhang, X., Abedini, A., Schmidt, A.M., and Raleigh, D.P. (2015). Islet amyloid polypeptide: structure, function, and pathophysiology. J. Diabetes Res. *2016*, 1–18.

11. Mukherjee, A., Morales-Scheihing, D., Butler, P.C., and Soto, C. (2015). Type 2 diabetes as a protein misfolding disease. Trends Mol. Med. *21*, 439–449.

12. Cao, P., Abedini, A., and Raleigh, D.P. (2013). Aggregation of islet amyloid polypeptide: from physical chemistry to cell biology. Curr. Opin. Struct. Biol. *23*, 82–89.

13. Zraika, S., Hull, R.L., Verchere, C.B., Clark, A., Potter, K.J., Fraser, P.E., Raleigh, D.P., and Kahn, S.E. (2010). Toxic oligomers and islet beta cell death: guilty by association or convicted by circumstantial evidence? Diabetologia *53*, 1046–1056.

14. Luca, S., Yau, W.M., Leapman, R., Tycko, R., and Tycko. (2007). Peptide conformation and supramolecular organization in amylin fibrils: constraints from solid-state NMR. Biochemistry *46*, 13505–13522.

15. Bedrood, S., Li, Y., Isas, J.M., Hegde, B.G., Baxa, U., Haworth, I.S., and Langen, R. (2012). Fibril structure of human islet amyloid polypeptide. J. Biol. Chem. *287*, 5235–5241.

16. Atsmon-Raz, Y., Wineman-Fisher, V., Baram, M., and Miller, Y. (2019). Unique inversion events of residues around the backbone in the turn domain of β-arches in amylin fibrils. ACS Chem. Neurosci. *10*, 1209–1213.

17. Wineman-Fisher, V., Tudorachi, L., Nissim, E., and Miller, Y. (2016). The removal of disulfide bonds in amylin oligomers leads to the conformational change of the 'native' amylin oligomers. Phys. Chem. Chem. Phys. *18*, 12438–12442.

18. Wineman-Fisher, V., Atsmon-Raz, Y., and Miller, Y. (2015). Orientations of residues along the β-arch of self-assembled amylin fibril-like structures lead to polymorphism. Biomacromolecules *16*, 156–165.

19. Cao, Q., Boyer, D.R., Sawaya, M.R., Ge, P., and Eisenberg, D.S. (2020). Cryo-EM structure and inhibitor design of human IAPP (amylin) fibrils. Nat. Struct. Mol. Biol. *27*, 653–659.

20. Cao, Q., Boyer, D.R., Sawaya, M.R., Abskharon, R., Saelices, L., Nguyen, B.A., Lu, J., Murray, K.A., Kandeel, F., and Eisenberg, D.S. (2021). Cryo-EM structures of hIAPP fibrils seeded by patient-extracted fibrils reveal new polymorphs and conserved fibril cores. Nat. Struct. Mol. Biol. *28*, 724–730.

21. Gallardo, R., Iadanza, M.G., Xu, Y., Heath, G.R., Foster, R., Radford, S.E., and Ranson, N.A. (2020). Fibril structures of diabetes-related amylin variants reveal a basis for surface-templated assembly. Nat. Struct. Mol. Biol. *27*, 1048–1056.

22. Röder, C., Kupreichyk, T., Gremer, L., Schfer, L.U., Pothula, K.R., Ravelli, R.B.G., Willbold, D., Hoyer, W., and Schröder, G.F. (2020). Cryo-EM structure of islet amyloid polypeptide fibrils reveals similarities with amyloid-β fibrils. Nat. Struct. Mol. Biol. *27*, 660–667.

23. Fitzpatrick, A.W.P., Falcon, B., He, S., Murzin, A.G., Murshudov, G., Garringer, H.J., Crowther, R.A., Ghetti, B., Goedert, M., and Scheres, S.H.W. (2017). Cryo-EM structures of tau filaments from Alzheimer's disease. Nature *547*, 185–190.

24. Falcon, B., Zhang, W., Murzin, A.G., Murshudov, G., Garringer, H.J., Vidal, R., Crowther, R.A., Ghetti, B., Scheres, S.H.W., and Goedert, M. (2018). Structures of filaments from Pick's disease reveal a novel tau protein fold. Nature *561*, 137–140.

25. Bansal, A., Schmidt, M., Rennegarbe, M., Haupt, C., Liberta, F., Stecher, S., Puscalau-Girtu, I., Biedermann, A., and Fändrich, M. (2021). AA amyloid fibrils from diseased tissue are structurally different from in vitro formed SAA fibrils. Nat. Commun. *12*, 1013.

26. Lövestam, S., Koh, F.A., van Knippenberg, B., Kotecha, A., Murzin, A.G., Goedert, M., and Scheres, S.H.W. (2022). Assembly of recombinant tau into filaments identical to those of Alzheimer's disease and chronic traumatic encephalopathy. Elife *11*, e76494. https://doi.org/10.7554/eLife.76494.

27. Zielinski, M., Röder, C., and Schröder, G.F. (2021). Challenges in sample preparation and structure determination of amyloids by cryo-EM. J. Biol. Chem. *297*, 100938.

28. Sawaya, M.R., Hughes, M.P., Rodriguez, J.A., Riek, R., and Eisenberg, D.S. (2021). The expanding amyloid family: structure, stability, function, and pathogenesis. Cell *184*, 4857–4873.

29. Zhang, X., Li, D., Zhu, X., Wang, Y., and Zhu, P. (2020). Structural characterization and cryo-electron tomography analysis of human islet amyloid polypeptide suggest a synchronous process of the hIAPP1-37 amyloid fibrillation. Biochem. Biophys. Res. Commun. *533*, 125–131.

30. Zivanov, J., Nakane, T., Forsberg, B.O., Kimanius, D., Hagen, W.J., Lindahl, E., and Scheres, S.H. (2018). New tools for automated high-resolution cryo-EM structure determination in RELION-3. Elife *7*, e42166.

31. Janson, J., Laedtke, T., Parisi, J.E., O'Brien, P., Petersen, R.C., and Butler, P.C. (2004). Increased risk of type 2 diabetes in Alzheimer disease. Diabetes *53*, 474–481.

32. Miklossy, J., Qing, H., Radenovic, A., Kis, A., Vileno, B., Làszló, F., Miller, L., Martins, R.N., Waeber, G., Mooser, V., et al. (2010). Beta amyloid and hyperphosphorylated tau deposits in the pancreas in type 2 diabetes. Neurobiol. Aging *31*, 1503–1515.

33. Peila, R., Rodriguez, B.L., and Launer, L.J.; Honolulu-Asia Aging Study (2002). Type 2 diabetes, APOE gene, and the risk for dementia and related pathologies: the Honolulu-Asia Aging Study. Diabetes *51*, 1256–1262.

34. Oskarsson, M.E., Paulsson, J.F., Schultz, S.W., Ingelsson, M., Westermark, P., and Westermark, G.T. (2015). In vivo seeding and cross-seeding of localized amyloidosis: a molecular link between type 2 diabetes and Alzheimer disease. Am. J. Pathol. *185*, 834–846.

35. Moreno-Gonzalez, I., Edwards Iii, G., Salvadores, N., Shahnawaz, M., Diaz-Espinoza, R., and Soto, C. (2017). Molecular interaction between type 2 diabetes and Alzheimer's disease through cross-seeding of protein misfolding. Mol. Psychiatry *22*, 1327–1334.

36. Schmidt, M., Rohou, A., Lasker, K., Yadav, J.K., Schiene-Fischer, C., Fändrich, M., and Grigorieff, N. (2015). Peptide dimer structure in an Aβ(1-42) fibril visualized with cryo-EM. Proc. Natl. Acad. Sci. USA *112*, 11858–11863.

37. Johnson, K.H., Westermark, P., Nilsson, G., Sletten, K., O'Brien, T.D., and Hayden, D.W. (1985). Feline insular amyloid: immunohistochemical and immunochemical evidence that the amyloid is insulin-related. Vet. Pathol. *22*, 463–468.

38. Rodriguez Camargo, D.C., Tripsianes, K., Buday, K., Franko, A., Göbl, C., Hartlmüller, C., Sarkar, R., Aichler, M., Mettenleiter, G., Schulz, M., et al. (2017). The redox environment triggers conformational changes and aggregation of hIAPP in Type II Diabetes. Sci. Rep. *7*, 44041. https://doi.org/10.1038/srep44041.

39. Wiltzius, J.J.W., Sievers, S.A., Sawaya, M.R., Cascio, D., Popov, D., Riekel, C., and Eisenberg, D. (2008). Atomic structure of the cross-β spine of islet amyloid polypeptide (amylin). Protein Sci. *17*, 1467–1474.

40. Zheng, S.Q., Palovcak, E., Armache, J.P., Verba, K.A., Cheng, Y., and Agard, D.A. (2017). MotionCor2: anisotropic correction of beam-induced motion for improved

cryo-electron microscopy. Nat. Methods *14*, 331–332.

41. Zhang, K. (2016). Gctf: real-time CTF determination and correction. J. Struct. Biol. *193*, 1–12.

42. He, S., and Scheres, S.H.W. (2017). Helical reconstruction in RELION. J. Struct. Biol. *198*, 163–176.

43. Emsley, P., Lohkamp, B., Scott, W.G., and Cowtan, K. (2010). Features and development of coot. Acta Crystallogr. D Biol. Crystallogr. *66*, 486–501.

44. Liebschner, D., Afonine, P.V., Baker, M.L., Bunkóczi, G., Chen, V.B., Croll, T.I., Hintze, B., Hung, L.W., Jain, S., McCoy, A.J., et al. (2019). Macromolecular structure determination using X-rays, neutrons and electrons: recent developments in Phenix. Acta Crystallogr. D Struct. Biol. *75*, 861–877.

45. Pettersen, E.F., Goddard, T.D., Huang, C.C., Couch, G.S., Greenblatt, D.M., Meng, E.C., and Ferrin, T.E. (2004). UCSF Chimera—a visualization system for exploratory research and analysis. J. Comput. Chem. *25*, 1605–1612.

46. Goddard, T.D., Huang, C.C., Meng, E.C., Pettersen, E.F., Couch, G.S., Morris, J.H., and Ferrin, T.E. (2018). UCSF ChimeraX: meeting modern challenges in visualization and analysis. Protein Sci. *27*, 14–25.

47. Delano, W.L. (2002). The PyMol molecular graphics system. Proteins Struct. Funct. Bioinf. *30*, 442–454.

48. Chen, V.B., Arendall, W.B., Headd, J.J., Keedy, D.A., Immormino, R.M., Kapral, G.J., Murray, L.W., Richardson, J.S., and Richardson, D.C. (2010). MolProbity: all-atom structure validation for macromolecular crystallography. Acta Crystallogr. D Biol. Crystallogr. *66*, 12–21.

STAR★METHODS

KEY RESOURCES TABLE

REAGENT or RESOURCE	SOURCE	IDENTIFIER
Chemicals, peptides, and recombinant proteins		
Human IAPP1-37	Shanghai Shending Biological Technology	P019030802
hexafluoroisopropanol (HFIP)	Sigma-Aldrich	105228-5G
Deposited data		
hIAPP fibril, SF, cryo-EM map	This paper	EMD: 33897
hIAPP fibril, TF-type1, cryo-EM map	This paper	EMD: 33902
hIAPP fibril, TF-type2, cryo-EM map	This paper	EMD: 33901
hIAPP fibril, TF-type3, cryo-EM map	This paper	EMD: 33903
hIAPP fibril, SF, coordinate	This paper	PDB: 7YKW
hIAPP fibril, TF-type1, coordinate	This paper	PDB: 7YL3
hIAPP fibril, TF-type2, coordinate	This paper	PDB: 7YL0
hIAPP fibril, TF-type3, coordinate	This paper	PDB: 7YL7
hIAPP fibril structure *in vitro* with SUMO-tag	Cao et al.[19]	PDB: 6VW2
hIAPP fibril structure *in vitro*	Gallardo et al.[21]	PDB: 6ZRF
hIAPP fibril structure *in vitro*	Röder et al.[22]	PDB: 6Y1A
hIAPP fibril structure seeded by patient-extracted fibrils	Cao et al.[20]	PDB: 7M61
hIAPP fibril structure seeded by patient-extracted fibrils	Cao et al.[20]	PDB: 7M62
hIAPP fibril structure seeded by patient-extracted fibrils	Cao et al.[20]	PDB: 7M64
hIAPP fibril structure seeded by patient-extracted fibrils	Cao et al.[20]	PDB: 7M65
Aβ fibril structure in absence of salt	Schmidt et al.[36]	PDB: 5AEF
Crystal structure of hIAPP core region	Wiltzius et al.[39]	PDB: 3DGJ
NMR structure of hIAPP monomer	Rodriguez Camargo et al.[38]	PDB: 5MGQ
Software and algorithms		
MotionCor2	Zheng et al.[40]	https://emcore.ucsf.edu/ucsf-software
Gctf	Zhang, K.[41]	https://www2.mrc-lmb.cam.ac.uk/download/gctf_v1-06-and-examples/
RELION	Zivanov et al.[42]	https://www3.mrc-lmb.cam.ac.uk/relion
COOT	Emsley et al.[43]	https://www2.mrc-lmb.cam.ac.uk/personal/pemsley/coot/
PHENIX	Liebschner et al.[44]	https://phenixonline.org/documentation/reference/real_space_refine.html
UCSF Chimera	Pettersen et al.[45]	https://www.cgl.ucsf.edu/chimera/
UCSF Chimera X	Goddard et al.[46]	http://rbvi.ucsf.edu/chimerax/
Pymol	Delano, W.L.[47]	https://www.pymol.org/pymol.html

RESOURCE AVAILABILITY

Lead contact

Further information and requests for resources should be directed to and will be fulfilled by the lead contact Ping Zhu (zhup@ibp.ac.cn).

Materials availability

This study did not generate new unique reagents.

Data and code availability

- The cryo-EM density map and corresponding atomic model generated in this work have been deposited at the EMDB database and PDB database and are publicly available as of the date of publication. Accession numbers are listed in the key resources table. This paper analyzes existing, publicly available data. These accession numbers for the datasets are listed in the key resources table.
- This paper does not report original code.
- Any additional information required to reanalyze the data reported in this paper is available from the lead contact upon request.

METHOD DETAILS

Sample preparation of hIAPP$_{1-37}$ amyloid

Human IAPP$_{1-37}$ was synthesized by Shanghai Shending Biological Technology, and the purity of the polypeptide (95%) was confirmed by high-performance liquid chromatography (HPLC) and mass spectrometry (MS). Lyophilized hIAPP$_{1-37}$ was first dissolved in hexafluoroisopropanol (HFIP) to a stock concentration of 2 mM. Aliquots of polypeptide stock solutions were pipetted into 1.5 mL centrifuge tubes, and the HFIP was evaporated in a fume hood at room temperature for 6-8 min. Then, the peptide was diluted with Milli-Q water to a concentration of 100 μM with ~2% HFIP for the fibril formation experiments. Samples were sonicated and incubated for a designated time at 37 °C with (or without) constant agitation (200 rpm) to form fibrils.

Thioflavin T (ThT) binding assay

Synthetic hIAPP monomers (10 μM) were adequately mixed with 9 μM ThT and added into a 96-well-plate with different buffer and salt concentration solutions: water, PBS buffer, NH_4Ac buffer, 0.5 mM NaCl, 50 mM NaCl, 150 mM NaCl. Samples were incubated at 37 °C for 15 hours with 650 r.p.m. linear shaking. ThT fluorescence signal was monitored using the EnVision Multilabel Plate Reader (PerkinElmer) at an excitation wavelength of 440 nm and an emission wavelength of 482 nm.

Effect of salt concentration on mature fibril morphology

Synthetic hIAPP monomers (10 μM) were incubated for a 15 hat 37 °C with constant agitation (200 rpm) in Milli-Q water to form mature fibrils. Subsequently, mature fibril samples were added to solutions with different final concentrations of NaCl: 0 mM, 0.1 mM, 50 mM, and 100 mM. The new solution was placed overnight at 4 °C to prevent further fibril growth. For comparison, the hIAPP monomers were also incubated in 100 mM NaCl solution to form mature fibrils first. The mature fibril samples were then diluted to different solutions with final concentrations of NaCl at 50 mM (by volume ratio 1:1 mixture with water), 0.1 mM (by dialysis to 0.1 mM NaCl), and 0 mM (by dialysis to water), respectively. The negative staining EM of the fibrils in different salt ion solutions were then observed under an electron microscope.

Negative-stain EM analysis of hIAPP amyloids

Samples for negative-stain electron microscopy were incubated on freshly glow-discharged carbon-coated copper grids for 1 min, and sample excess was removed by blotting on filter paper. Grids were stained with 1% (w/v) uranyl acetate for 1 min, and the excess uranyl acetate was blotted off. Grids were examined with a Tecnai Spirit transmission electron microscope (FEI) at an acceleration voltage of 120 kV.

Cryo-electron microscopy sample preparation of hIAPP amyloids

Aliquots of 3 μL of fibril solutions (growing up to 9 h) were dropped onto freshly glow-discharged holey carbon grids (Quantifoil Cu R2/1,300 mesh), blotted with filter paper for 3 s to remove an excess sample, and vitrified by plunging into liquid nitrogen-cooled liquid ethane using Vitrobot Mark IV (Thermo Fisher) at 4 °C and 100% humidity. The grids were transferred to a Titan Krios electron microscope (Thermo Fisher) operating at 300 kV. Micrographs were collected using a Gatan-K2 Summit counting camera (Gatan Company) in super-resolution mode with an energy filter in a calibrated pixel size of 1.04 Å/pixel. A total of 3,200

micrographs were recorded with total electron doses of 60 $e^{-}/Å^{2}$ in 32 frames. The defocus value target was set from 1.5 to 2 μm.

Helical reconstruction

The frames in each movie were aligned and summed to generate a micrograph by using Motioncorr2.[40] Summed micrographs were used to determine to defocus values by Gctf.[41] Filaments were manually picked in Relion 3.0[30] based on their distinct morphological characteristics. Particles of SF and TF were extracted with different box sizes and overlapped. TF was segmented into 264 × 264 pixel boxes with an interbox distance of 23.5 Å. SF was segmented into 208 × 208 pixel boxes with an interbox distance of 14.4 Å. The two types of fibrils were processed separately. T = 4 was used for multiple rounds of 2D classification, which showed a clear obvious β-sheet pattern. The 2D classification results also showed asymmetrical twisting of the SF and pseudo C2 symmetrical twisting of the TF. The *relion_helix_toolbox* command was used to generate a 60 Å low-pass filtered cylinder as the initial model. After three-dimensional classification with K = 1 and T = 10, the selected 3D result was used as the new initial model to perform another three-dimensional classification with K = 4 and T = 20. The classification results showed that SF was an asymmetric dimer and TF was a 2^{1} symmetric tetramer. After 3D classification of TF datasets, three types of TF structures with similar shapes and different helical states were obtained: TF-type 1 (179.28 helical twist, 2.35 Å helical rise), TF-type 2 (179.3 helical twist, 2.35 Å helical rise), and TF-type 3 (179.41 helical twist, 2.35 Å helical rise). To further improve the resolution, the 3D classes with good SF and TF features were selected for 3D refinement.[42] For SF, helical rise and twist converged to 4.7 Å and −1.22°, and finally, we obtained high-resolution structures of SF at 3.6 Å resolution. For TF, the 3D map did not show clear side chain densities, probably due toheterogeneity and flexibility. To optimize the resolution of the TF datasets, we provided a T value of 50 and fixed helical parameters in 3D refinement using their respective 3D maps as reference maps in the 3D refinement process. All models were masked (SF, 10% of Z length; TF (type 1, 2, 3), 15% of Z length) and postprocessed in Relion. Finally, high-resolution maps of the three types of TF were acquired at resolutions of 3.3 Å, 3.2 Å, and 3.3 Å and showed clear side chain densities. For the S-like shaped fibril, only 968 particles were extracted with 200 × 200 pixel boxes by manual pick for small box 2D-Classification. Whereafter, those particles were re-extracted with 600 × 600 pixel boxes for large box 2D-Classification. 3D classification was performed using a T value of 4 and N value of 1 with small box.

Model building and refinement

The sharpened and masked 3D density maps of two filaments were used to manually build atomic models in Coot.[43] Based on the flexibility of the swing of the disulfide bond at the N-terminus of the peptide chain and protofilament interactions, we determined the orientation of the N-terminus to the C-terminus of each monomer and traced the main chain. Then, residues with clear densities, such as Phe and His, were marked, and reasonable atomic models were built. The models were then subjected to PHENIX[44] for refinement to obtain the final models. After model evaluation using MolProbity,[48] molecular graphics, and further analyses were performed using Chimera,[45] ChimeraX,[46] and PyMOL.[47]

QUANTIFICATION AND STATISTICAL ANALYSIS

The proportions of particle belonging to different polymorphisms in Figure 2 was counted by Relion.[30] Specifically, fibril particle auto-picking command in Relion was used to pick all fibrils with the same inter-box distance, then extracted particles were classified by 2D-classificition to analyse the particle proportions which belong to the same polymorphism.